Journal of
Applied Remote Sensing

RemoteSensing.SPIEDigitalLibrary.org

Reweighted mass center based object-oriented sparse subspace clustering for hyperspectral images

Han Zhai
Hongyan Zhang
Liangpei Zhang
Pingxiang Li

SPIE.

Han Zhai, Hongyan Zhang, Liangpei Zhang, Pingxiang Li, "Reweighted mass center based object-oriented sparse subspace clustering for hyperspectral images," *J. Appl. Remote Sens.* **10**(4), 046014 (2016), doi: 10.1117/1.JRS.10.046014.

Reweighted mass center based object-oriented sparse subspace clustering for hyperspectral images

Han Zhai,[a] Hongyan Zhang,[a,b,*] Liangpei Zhang,[a,b] and Pingxiang Li[a,b]
[a]Wuhan University, State Key Laboratory of Information Engineering in Surveying, Mapping, and Remote Sensing, No. 129 Luoyu Road, Wuhan 430079, China
[b]Wuhan University, Collaborative Innovation Center for Geospatial Technology, No. 129 Luoyu Road, Wuhan 430079, China

Abstract. Considering the inevitable obstacles faced by the pixel-based clustering methods, such as salt-and-pepper noise, high computational complexity, and the lack of spatial information, a reweighted mass center based object-oriented sparse subspace clustering (RMC-OOSSC) algorithm for hyperspectral images (HSIs) is proposed. First, the mean-shift segmentation method is utilized to oversegment the HSI to obtain meaningful objects. Second, a distance reweighted mass center learning model is presented to extract the representative and discriminative features for each object. Third, assuming that all the objects are sampled from a union of subspaces, it is natural to apply the SSC algorithm to the HSI. Faced with the high correlation among the hyperspectral objects, a weighting scheme is adopted to ensure that the highly correlated objects are preferred in the procedure of sparse representation, to reduce the representation errors. Two widely used hyperspectral datasets were utilized to test the performance of the proposed RMC-OOSSC algorithm, obtaining high clustering accuracies (overall accuracy) of 71.98% and 89.57%, respectively. The experimental results show that the proposed method clearly improves the clustering performance with respect to the other state-of-the-art clustering methods, and it significantly reduces the computational time. © *2016 Society of Photo-Optical Instrumentation Engineers (SPIE)* [DOI: 10.1117/1.JRS.10.046014]

Key words: hyperspectral image; object-oriented clustering; sparse subspace clustering; mean shift; distance reweighted mass center learning.

Paper 16596 received Aug. 9, 2016; accepted for publication Oct. 27, 2016; published online Nov. 23, 2016.

1 Introduction

Hyperspectral imaging can obtain the continuous spectra of land-cover materials with a nanometer precision, which represents a function of the wavelength with a large spectral range and a high spectral resolution.[1–3] Every pixel in a hyperspectral image (HSI) is represented by hundreds of values, and each value corresponds to a different narrow wavelength.[4] In this way, HSIs provide richer spectral information than multispectral imagery, to support the fine recognition of various land-cover materials, and they have opened up new remote sensing application fields, such as geology,[5] ecological environment monitoring,[6,7] urban planning,[8] and precision agriculture.[9] Among these applications, a commonly used fundamental technique is clustering. The clustering label can be decided by a similarity measure, which means that pixels with the same label are similar and those with different labels are dissimilar. However, due to the large spectral variations and spatial complexities, it is usually a very challenging task to cluster HSIs.

The pixel-based clustering methods have experienced a long period of development. Typical examples include the classical centroid clustering methods, such as k-means [10] and fuzzy c-means (FCM),[11,12] density-based methods, such as the clustering by fast search and find of density peaks algorithm (CFSFDP),[13] the more complex biological methods, such as unsupervised remote sensing image classification using an artificial immune network,[14] and the graph-based methods, such as spectral local best-fit flats.[15,16] In recent years, some improved variations

---

[*] Address all correspondence to: Hongyan Zhang, E-mail: zhanghongyan@whu.edu.cn

1931-3195/2016/$25.00 © 2016 SPIE

of the traditional clustering models have been proposed, such as the unsupervised classification of hyperspectral imaging data using projection pursuit and the Markov random field segmentation model.[17] However, due to the uniform distribution of the feature space of HSIs, these methods still cannot achieve satisfactory segmentation accuracies.

More recently, the sparse subspace clustering (SSC) algorithm has been proposed[18,19] and has been successfully applied to cluster HSIs, showing great potential.[20,21] By taking full advantage of the high spectral correlation and the spatial neighborhood information, the spectral–spatial sparse subspace clustering (S^4C) algorithm has significantly improved the performance of SSC.[20,22] However, as in most pixel-level clustering methods, the S^4C method faces some limitations: (1) it produces a characteristic and inconsistent salt-and-pepper clustering map; (2) it is not capable of making full use of the different neighborhood relationships; and (3) it often results in high computational complexity.

To overcome these shortcomings, in recent years, researchers have paid attention to the object-oriented clustering methods, which simultaneously utilize the spectral and spatial information to fully exploit the inherent attributes and structure of HSIs to obtain a better clustering performance.[23–25] For example, some researchers have used k-means or FCM to cluster objects obtained by segmentation to improve the precision to a certain degree.[26–32] In addition, the object-oriented semantic clustering algorithm for HSIs using the probabilistic latent semantic analysis model coupled with neighborhood spatial information was proposed and found to outperform the classical pixel-based clustering algorithms.[33] All these methods have shown that the object-oriented methods are superior to the pixel-based methods from the following aspects.[34–36] First, with the help of image objects, spatial semantic information is incorporated into the clustering scheme, which can effectively relieve the influence of salt-and-pepper noise and fully utilize the spatial information of the HSI. Second, the computational complexity is significantly reduced because of the direct operation on objects rather than pixels, which opens up great potential for real remote sensing applications.

In view of this, this paper proposes a reweighted mass center based object-oriented sparse subspace clustering (RMC-OOSSC) algorithm for HSIs to fully exploit the potential of the SSC model and overcome the defects of the pixel-based methods. The basic ideas and contributions of this paper can be summarized as follows. First, the effective and robust mean-shift method is adopted to oversegment the HSI to obtain meaningful image objects,[25,37] acquiring homogeneous areas and accurate boundary information by considering both the spectral and spatial information of the HSI. In the clustering process, each object is treated as a particular pixel, as in the pixel-based clustering scheme. In this way, the computational complexity is significantly reduced. Second, a distance reweighted mass center learning model is presented to extract the representative and discriminative features for each object, which incorporates the spatial neighborhood information to reduce the influence of salt-and-pepper noise and simultaneously exploit the spectral–spatial structure of the HSI. Third, the extracted objects are assigned into different clusters with the weighted SSC model, which can effectively relieve the spectral noise problem.

However, the proposed algorithm still has room for improvement. For instance, more meaningful features of the segmentation objects could be utilized in the clustering procedure, which may provide more discriminative capability. In addition, the number of objects has a large influence on the final clustering performance, and the RMC-OOSSC algorithm cannot adaptively determine this. All these issues will be addressed in our future work.

The rest of this paper is organized as follows. Section 2 reviews the classical SSC model. Section 3 introduces the proposed RMC-OOSSC algorithm for HSIs. In Sec. 4, the experimental results of the proposed RMC-OOSSC algorithm are presented for two widely used HSI datasets. Section 5 draws the conclusions and summarizes our future work.

2 Classical Sparse Subspace Clustering Model

2.1 *Sparse Representation*

In the sparse representation model, a target signal can be approximated by a linear or an affine combination of a few elements from an overcomplete dictionary, which can usually be represented in the form of $\mathbf{A} \in R^{D\times K}$ with $D < K$. The signal $\mathrm{t} \in R^D$ can then be approximately represented by multiplying the dictionary $\mathbf{A}$ with a coefficient vector $\alpha \in R^K$. As only a few entries in α are nonzero, it is called a sparse vector, which can be obtained by solving the following optimization problem:

$$\alpha = \arg\ \min \|\alpha\|_0 \quad \text{s.t. } \mathrm{t} = \mathbf{A}\alpha + \zeta, \tag{1}$$

where $\zeta \in R^D$ is the representation error vector. Because the ℓ_0-norm, which counts the number of nonzero elements of α, is usually an nondeterministic polynomial (NP)-hard combinatorial problem, one of the following two strategies is usually adopted: a greedy pursuit-based algorithm or an ℓ_1-norm convex relaxation algorithm.[18]

2.2 *Sparse Subspace Clustering Model for Hyperspectral Images*

The classical SSC model utilizes the self-expressiveness property of the data.[18,19] That is to say, each sample is regarded as lying in a union of subspaces, which the dataset belongs to, with each subspace corresponding to a class or a cluster.[38] In this way, each target signal can be approximately represented by other samples from the same subspace, which corresponds to the sparsest representation solution. The sparse representation coefficients are then utilized to segment these samples into different clusters corresponding to separate subspaces.

For an HSI dataset, although pixels of the same land-cover type may have varying reflection and absorption features because of the different imaging conditions, they will lie in the same subspace. That is to say, each pixel lies in an exact subspace of the union of the linear or affine subspaces $\{C_i\}_{i=1}^l$, where l represents the number of subspaces. Therefore, the SSC scheme for HSIs is reasonable. Specifically, the 3-D HSI cube can be represented as a 2-D matrix $\mathbf{Y} = [\mathbf{Y}_1, \mathbf{Y}_2, \cdots, \mathbf{Y}_{MN}]$, $\mathbf{Y} \in R^{D\times MN}$, with each column representing a high-dimensional vector corresponding to a certain hyperspectral pixel, where D refers to the dimension of each vector, M represents the width of the HSI data, and N stands for the height of the data. Considering the similar energy of hyperspectral pixels, it is more practical to adopt the affine subspace to model HSIs because it applies a constraint to the points lying in the union of the subspaces. Then, with the HSI dataset itself being the dictionary, the SSC scheme models the sparse representation procedure as follows:

$$\min_{\mathbf{C}} \|\mathbf{C}\|_0 + \frac{\lambda}{2}\|\mathbf{N}\|_F^2 \quad \text{s. t. } \mathbf{Y} = \mathbf{YC} + \mathbf{N}, \quad \mathrm{diag}(\mathbf{C}) = 0, \quad \mathbf{C}^T 1 = 1, \tag{2}$$

where $\mathbf{C} \in R^{MN\times MN}$ is the coefficient matrix, $\mathbf{N} \in R^{D\times MN}$ is the representation error matrix, and parameter λ is the tradeoff between the sparsity of the coefficient and the magnitude of the noise. The constraint $\mathrm{diag}(\mathbf{C}) = 0$ is used to eliminate the trivial solution of writing a point as an affine combination of itself.[18,39–42] In addition, the constraint $\mathbf{C}^T 1 = 1$ means that the affine subspace model is adopted, where $1 \in R^{MN}$ is a vector whose elements are all ones. Although ℓ_0-norm minimization is the most direct application of sparse theory, it is usually an NP-hard problem in practice. Therefore, tightest convex surrogate ℓ_1-norm minimization is usually adopted, which faithfully seeks the representative atoms from the same subspace of the target hyperspectral pixel.[43–45] The sparse representation model can then be built as follows:

$$\min_{\mathbf{C},\mathbf{N}} \|\mathbf{C}\|_1 + \frac{\lambda}{2}\|\mathbf{N}\|_F^2 \quad \text{s.t. } \mathbf{Y} = \mathbf{YC} + \mathbf{N}, \quad \mathrm{diag}(\mathbf{C}) = 0, \quad \mathbf{C}^T 1 = 1. \tag{3}$$

This model can be easily solved by the alternating direction method of multipliers (ADMM). The sparse coefficient matrix $\mathbf{C}$ is then utilized to construct the similarity graph $\tilde{\mathbf{W}} \in R^{MN\times MN}$ in a symmetrization form, with each element standing for the similarity between pixel i and pixel j, which is also called the ℓ_1-direct weighted graph:

$$\tilde{\mathbf{W}} = |\mathbf{C}| + |\mathbf{C}|^T. \tag{4}$$

In this way, the connection of the graph can be effectively strengthened to guarantee that the pixels can be correctly segmented into the corresponding separate subspaces. Finally, spectral clustering is applied to obtain the clustering result.[46–50]

3 Reweighted Mass Center Based Object-Oriented Sparse Subspace Clustering Model for Hyperspectral Images

Directly applying SSC at the pixel level is usually affected by the following problems: (1) there is a huge amount of salt-and-pepper noise within classes; (2) different neighborhood relationships cannot be used; and (3) the computational complexity is huge. Therefore, an object-oriented strategy is to be preferred. For the proposed RMC-OOSSC algorithm, there are three main steps: (1) image object segmentation; (2) unsupervised mass center learning based feature extraction; and (3) the clustering operation.

3.1 *Image Segmentation*

For the object-oriented image analysis methods, extracting meaningful objects is the first and key step, and the quality of the extracted objects greatly affects the precision of the clustering result.[51–53] In practice, image segmentation methods are usually adopted to realize the above purpose and can be regarded as the process of partitioning the image into nonintersecting homogeneous regions.[24,37]

In order to obtain high-quality image objects to guarantee that each image object is pure, various properties of HSIs should be comprehensively considered in the segmentation scheme, and the oversegmentation strategy is adopted to eliminate mixed objects in this paper. Second, the segmentation should be robust to noise and singular points. Third, the segmentation method should be powerful enough to effectively segment arbitrarily structured feature spaces. Considering all the above aspects, the mean-shift segmentation method is adopted because of its robustness and ability to make full use of the spectral and spatial structure information to obtain accurate and ideal homogeneous objects.[37]

Mean shift is a nonparametric density-estimation technique, which is based on Parzen window-based kernel density estimation. With q data points x_i $(i = 1, \dots, q)$ in the D-dimensional feature space, the kernel density estimator at point x can be defined as follows:[25,37]

$$\hat{f}_{h,K}(x) = \frac{c_{k,D}}{qh^D} \sum_{i=1}^{q} k\left(\left\| \frac{x - x_i}{h} \right\|^2\right), \tag{5}$$

where $c_{k,D}$ is a normalization constant, h is the bandwidth parameter, and $k(\cdot)$ is the kernel profile, which models how strongly the data points are taken into account for the estimation.[25,37] Then, through differentiating Eq. (5) and decomposing to two product terms, as in Eq. (6), the mean-shift analysis finds the modes of this density, which are located along the gradient $\nabla f(x) = 0$ and are the local maxima of the density function $f(x)$:[37]

$$\hat{\nabla} f_{h,K}(x) = \frac{2}{h^2 c} \hat{f}_{h,G}(x) \cdot m_{h,G}(x), \tag{6}$$

where c is the normalization constant, defined as $c = c_{g,D}/c_{k,D}$, with $c_{g,D}$ being its normalization parameter, and the profile of kernel G is defined as $g(x) = -k'(x)$.[25,37] The first term in Eq. (6) is the density estimation at x with kernel G, and the second term is the mean-shift vector. These terms are formulated as follows:

$$\hat{f}_{h,G}(x) = \frac{c_{g,D}}{qh^D} \sum_{i=1}^{q} g\left(\left\| \frac{x - x_i}{h} \right\|^2\right), \tag{7}$$

$$m_{h,G}(x) = \frac{\sum_{i=1}^{q} x_i \cdot g\left(\left\| \frac{x - x_i}{h} \right\|^2\right)}{\sum_{i=1}^{q} g\left(\left\| \frac{x - x_i}{h} \right\|^2\right)} - x. \tag{8}$$

From Eq. (8), it can be easily found that the mean shift is the difference between the weighted means, with the kernel $g(\cdot)$ being used as the weights and x is the center of the kernel window. In fact, the mean-shift vector always moves toward the direction of maximum increase in the density. That is to say, the local mean is shifted toward the region in which the majority of the points reside, until reaching a stationary point called the mode.[25,37]

In essence, the mean-shift segmentation is a straightforward extension of the discontinuity preserving smoothing algorithm that can obtain accurate and ideal homogeneous regions, which are treated as objects, as shown in Fig. 1. With x_i and z_i, $i = 1, \cdots, n$ representing the D-dimensional input and filtered hyperspectral pixels in the joint spatial–spectral domain, respectively, L_i standing for the label of the i'th pixel, H denoting the number of clusters or objects, h_s being the threshold of the spatial domain, and h_r representing the threshold of the spectral domain, the mean-shift method contains the following main steps:

1. Run the mean-shift filtering procedure for the image and store all the information about the D-dimensional convergence point in z_i.
2. Delineate the clusters $\{C_f\}_{f=1,\cdots,H}$ in the joint domain by grouping together all of z_i, which are closer than h_s in the spatial domain and h_r in the spectral domain, i.e., concatenate the basins of attraction of the corresponding convergence points.
3. Assign a label to each pixel: $L_i = \{f | z_i \in C_f, i = 1 \cdots, MN\}$.
4. Optional: Eliminate spatial regions containing less than η pixels, where η denotes the minimum size of object.

3.2 *Unsupervised Mass Learning-Based Feature Extraction*

After image segmentation, it is necessary to extract representative and discriminative features for each object. Indeed, each object can be seen as a convex hull consisting of all the pixels within the object. An intuitive idea is to extract the center of mass of each convex hull, because the mass center can represent the common attributes of all the pixels in the convex hull and can relieve the influence of salt-and-pepper noise, as shown in Fig. 2. Considering that no prior knowledge or label information is available, an unsupervised mass center learning model is proposed here, which is named the distance reweighted mass center learning model. This model takes full advantage of the correlations between each pixel and the corresponding center, which can effectively reduce the sum of squared error between pixels and centers. The distance reweighted mass center learning model is formulated as follows:

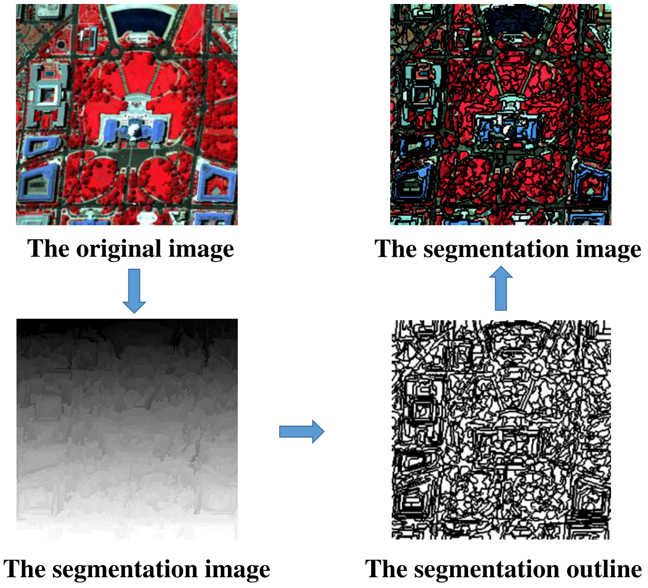

Fig. 1 The segmentation process. Through oversegmentation of the original hyperspectral image, the meaningful objects can be obtained.

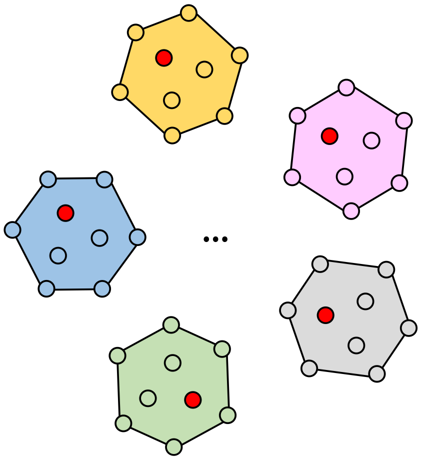

Fig. 2 The convex hull consists of all the pixels within the object, with the red point denoting its center of mass.

$$\bar{y}_f^{(k+1)} = \sum_{j=1}^{s} \frac{y_j}{\left\| \bar{y}_f^{(k)} - y_j \right\|_F^2}, \tag{9}$$

where $\bar{y}_f^{(k)}$ represents the mass center spectral signal of the f'th object in the k'th iteration, y_j stands for a hyperspectral pixel within the object, and s denotes the number of pixels located within the f'th object, and is usually called the "size" of the object. Specifically, the mass center can be learned through an iterative process, with the mean spectrum of each object utilized as the initial value. The distance between each pixel and the center is then used to calculate the corresponding weight to refresh the mass center of the convex hull until the difference between the new mass center and the old one is smaller than the predefined error tolerance τ. In this way, a representative feature of high quality can be extracted because it effectively reduces the difference between each pixel within the convex hull and the mass center. Meanwhile, it fully exploits the spectral–spatial structure attributes of the HSI and can effectively distinguish different land-cover materials.

Compared with the spectral feature in the pixel-based clustering methods, the mass center spectra have the following superiorities: (1) through calculating the center of mass, the influence of singular points and noise can be reduced to a large degree; (2) the mass center spectra can better satisfy the affine subspace model because the influence of singular points has been mitigated; and (3) it is natural for the mass center spectra to consider neighborhood information in the extraction procedure so that the spatial information is fully used. That is to say, the mass center spectra are spectral–spatial features, so that they are more meaningful and discriminative and can significantly reduce the representation bias in the sparse representation procedure.[54]

3.3 *Object-Oriented Sparse Subspace Clustering with a Weighting Scheme*

Considering the high correlations among the mass center spectra, it is necessary to add a constraint to help the SSC scheme choose the corresponding atoms with the highest correlation to represent the signals.[22] As with the pixel-based SSC scheme, the data matrix consisting of these mass center spectra is utilized as the self-representation dictionary. Then, by imposing greater weights on the highly correlated atoms and smaller weights on the less correlated atoms, the SSC model with a weighting scheme is constructed to ensure that the atoms with high correlation occupy the dominant place in the sparse representation process.[21] In this way, a more accurate representation coefficient matrix can be obtained, which directly contributes to improving the final clustering accuracy.

Specifically, the representation coefficient matrix can be obtained by solving the following sparse optimization problem:

$$\min_{\bar{\mathbf{C}},\mathbf{N}} \|\mathbf{W}\bar{\mathbf{C}}\|_1 + \frac{\lambda}{2}\|\mathbf{N}\|_F^2 \quad \text{s.t. } \bar{\mathbf{Y}} = \bar{\mathbf{Y}}\,\bar{\mathbf{C}} + \mathbf{N}, \quad \operatorname{diag}(\bar{\mathbf{C}}) = 0, \quad \bar{\mathbf{C}}^T 1 = 1, \tag{10}$$

where $\bar{\mathbf{Y}} \in R^{D\times H}$ represents the object signals, with each column corresponding to a mass center spectrum $\bar{y}$, H stands for the number of objects obtained by the image segmentation, and $\bar{\mathbf{C}} \in R^{H\times H}$ denotes the corresponding sparse representation matrix. The weighted matrix $\mathbf{W}$ is defined in the following way:

$$\mathbf{W}_{i,j} = \frac{1}{\|\bar{y}_i - \bar{y}_j\|_2^2 + \gamma} i, j = 1,2, \cdots, H, \quad i \neq j, \tag{11}$$

where $\bar{y}_i$ and $\bar{y}_j$ represent the i'th mass center spectrum and the j'th mass center spectrum, respectively. The normalization parameter γ is a very small constant, which can be set as 0.001 in practice, to avoid the weight of two extremely similar adjacent objects being super large. The diagonal elements of $\mathbf{W}$ are all zeros to avoid a trivial solution. The corresponding weight is then normalized by the following formulation to guarantee that the value will fall into the range of 0 to 1:

$$\mathbf{W}_{i,j} = \frac{\mathbf{W}_{i,j}}{\mathbf{W}_{i,\cdot}} i, j = 1,2, \ldots, H, \tag{12}$$

where $\mathbf{W}_{i,\cdot}$ is the i'th row of the weighted matrix $\mathbf{W}$.

Equation (10) can be efficiently solved with the ADMM in the following way.[55–61] Through introducing an auxiliary matrix $\mathbf{A} \in R^{H\times H}$ with the same size as the sparse coefficient matrix $\bar{\mathbf{C}}$ to the objective function to separate the variables, along with two penalty terms corresponding to $\mathbf{A}^T 1 = 1$ and $\mathbf{A} = \bar{\mathbf{C}} - \operatorname{diag}(\bar{\mathbf{C}})$, Eq. (10) is transformed into the Lagrange function as follows:

$$\begin{aligned} L(\bar{\mathbf{C}}, \mathbf{A}, \delta, \boldsymbol{\Delta}) = {} & \|\mathbf{W}\bar{\mathbf{C}}\|_1 + \frac{\lambda}{2}\|\bar{\mathbf{Y}} - \bar{\mathbf{Y}}\mathbf{A}\|_F^2 + \frac{\rho}{2}\|\mathbf{A}^T 1 - 1\|_2^2 \\ & + \frac{\rho}{2}\|\mathbf{A} - [\bar{\mathbf{C}} - \operatorname{diag}(\bar{\mathbf{C}})]\|_F^2 + \delta^T(\mathbf{A}^T 1 - 1) + \operatorname{tr}\{\boldsymbol{\Delta}^T[\mathbf{A} - \bar{\mathbf{C}} + \operatorname{diag}(\bar{\mathbf{C}})]\}, \end{aligned} \tag{13}$$

where $\operatorname{tr}(\cdot)$ denotes the trace operator of a given matrix, which sums up all the elements along the major diagonal line.

Each target variable can then be alternately updated in the iterative procedure as follows: (1) update $\mathbf{A}$ by Eq. (14), with the other four variables fixed; (2) update $\bar{\mathbf{C}}$ by fixing the other variables in Eq. (15); (3) update δ and $\boldsymbol{\Delta}$ with $\mathbf{A}$ and $\bar{\mathbf{C}}$ using Eqs. (16) and (17). Repeat these steps until convergence is achieved or the number of iterations exceeds the maximum iteration number. Specifically, convergence is achieved when we have $\|\mathbf{A}^{(k)^T} 1 - 1\|_\infty \leq \varepsilon$, $\|\mathbf{A}^{(k)} - \bar{\mathbf{C}}^{(k)}\|_\infty \leq \varepsilon$, $\|\mathbf{A}^{(k)} - \mathbf{A}^{(k-1)}\|_\infty \leq \varepsilon$, where ε denotes the predefined error tolerance for the primal and dual residuals:

$$(\lambda\bar{\mathbf{Y}}^T\bar{\mathbf{Y}} + \rho \mathrm{I} + \rho 11^T + \rho \mathrm{I})\mathbf{A}^{(k+1)} = \lambda\bar{\mathbf{Y}}^T\bar{\mathbf{Y}} + \rho\bar{\mathbf{C}}^{(k)} + \rho(11^T + \bar{\mathbf{C}}^{(k)}) - 1\delta^{(k)^T} - \boldsymbol{\Delta}^{(k)} \tag{14}$$

$$\bar{\mathbf{C}}^{(k+1)} = \mathbf{W}[\mathbf{J} - \operatorname{diag}(\mathbf{J})], \quad \mathbf{J} = \Gamma_{\frac{1}{\rho}}\left(\mathbf{A}^{(k+1)} + \frac{\boldsymbol{\Delta}^{(k)}}{\rho}\right), \tag{15}$$

$$\delta^{(k+1)} = \delta^{(k)} + \rho[\mathbf{A}^{(k+1)^T} 1 - 1], \tag{16}$$

$$\boldsymbol{\Delta}^{(k+1)} = \boldsymbol{\Delta}^{(k)} + \rho[\mathbf{A}^{(k+1)} - \bar{\mathbf{C}}^{(k+1)}], \tag{17}$$

where $\Gamma_{\frac{1}{\rho}}(\cdot)$ is the shrinkage-thresholding operator: $\Gamma_{\frac{1}{\rho}}(v) = (|v| - \frac{1}{\rho})_+ \operatorname{sgn}(v)$, where the operator $(\cdot)_+$ returns its arguments if it is non-negative and returns zero otherwise. The sparse coefficient matrix is then used to build the similarity graph in the same way as SSC. The cluster labels are then obtained by applying spectral clustering to it.

Table 1 RMC-OOSSC algorithm for hyperspectral images.

```
Input:
(1) A 2-D matrix of the HSI containing a set of points $\{y_i\}_{i=1}^{MN}$ in a union of $l$ affine subspaces $\{C_i\}_{i=1}^{l}$;
(2) Parameters, including the cluster number $l$ and regulation parameters $\lambda$ and $\rho$.
Main algorithm:
(1) Apply the mean-shift segmentation to obtain meaningful objects;
(2) Calculate the mass center spectra of the objects with Eq. (9);
(3) Calculate the weighted matrix $\mathbf{W}$ with Eq. (11) and normalize it with Eq. (12);
(4) Construct the sparse optimization model (10) and solve it to obtain the sparse coefficient matrix $\bar{\mathbf{C}}$ using
    ADMM;
(5) Normalize the columns of $\bar{\mathbf{C}}$ as $\bar{\mathbf{C}}_i \leftarrow \frac{\bar{\mathbf{c}}_i}{\|\bar{\mathbf{c}}_i\|_\infty}$;
(6) Construct the similarity graph with Eq. (4);
(7) Apply spectral clustering to the similarity graph to obtain the labels of the image objects;
(8) Label each pixel with the corresponding image object to obtain the final clustering result.
Output:
A 2-D matrix which records the labels of the clustering result of the HSI.
```

It should be noted that the cluster labels correspond to objects rather than pixels. An inverse mapping process from objects to pixels is therefore necessary. Based on the mechanism of segmentation, each object corresponds to a homogenous area. That is to say, all the pixels within it should share the same label as the corresponding object. Therefore, with the help of the spatial position information, it is easy to label each pixel according to the corresponding object. In this way, the final clustering result can be obtained.

3.4 *Flowchart*

The proposed RMC-OOSSC algorithm can be summarized, as shown in Table 1. The flowchart of the proposed RMC-OOSSC algorithm is given in Fig. 3.

4 Experimental Results and Discussion

4.1 *Data and Study Area*

Two widely used hyperspectral datasets were utilized to evaluate the performance of the proposed RMC-OOSSC algorithm: the University of Pavia dataset and the Washington, DC, Mall dataset.

The first experimental dataset was acquired by the Reflective Optics System Imaging Spectrometer (ROSIS) sensor during a flight campaign over Pavia, Northern Italy. The image is of a size of $610 \times 340 \times 103$ and its spatial resolution is 1.3 m. A typical area was used as the test data, with the size of $200 \times 100 \times 103$,[22] containing eight main land-cover classes: metal sheet, asphalt, meadows, trees, bare soil, bitumen, bricks, and shadows. Figure 4 shows the false-color image, the ground truth, and the spectral curves of the eight land-cover classes. Generally speaking, this image is difficult to cluster because the spectral signals of some classes are very similar, such as meadows and bitumen, which can be easily observed in Fig. 4.

The second experimental dataset was acquired by the Hyperspectral Digital Imagery Collection Experiment (HYDICE) sensor over the Washington, DC, Mall, United States, at a size of 1208×307, with 191 bands used in the experiment. As in the former experiment,

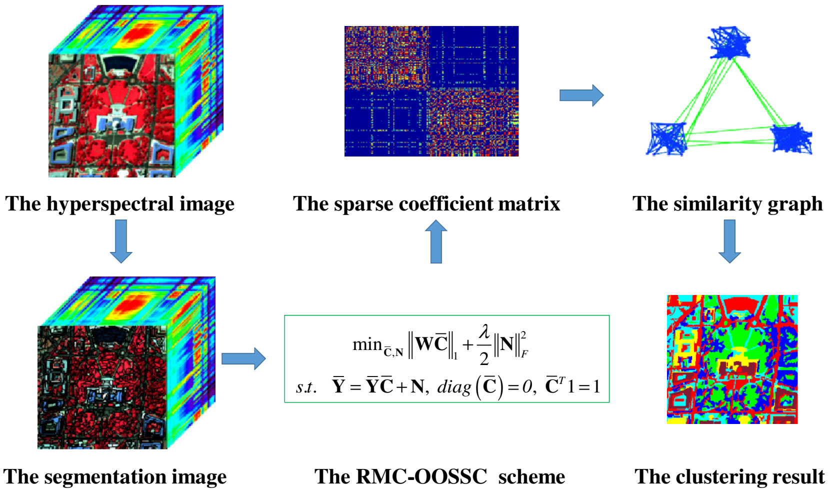

Fig. 3 The flowchart of the proposed RMC-OOSSC algorithm.

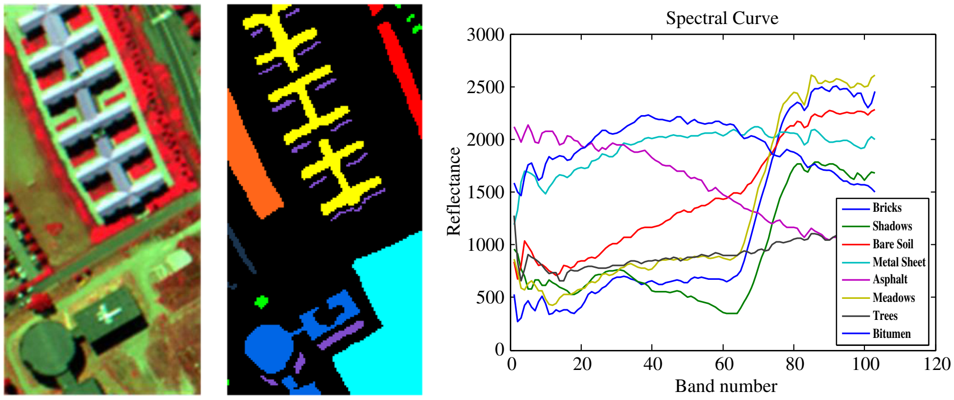

(a) (b) (c)

Fig. 4 ROSIS University of Pavia image: (a) the false-color image (RGB 102, 56, 31), (b) the ground truth, and (c) the spectral curves of the eight land-cover classes.

we used a typical area for the test of 256 × 257, containing six main land-cover classes: water, grass, trees, square, roof, and road. This dataset has a more complex distribution of land-cover classes, and the spectral signals of some classes are very similar, such as trees and grass, which leads to a more challenging task for the clustering. The spectral curves of the six land-cover classes are shown in Fig. 5, along with the false-color image and the ground truth.

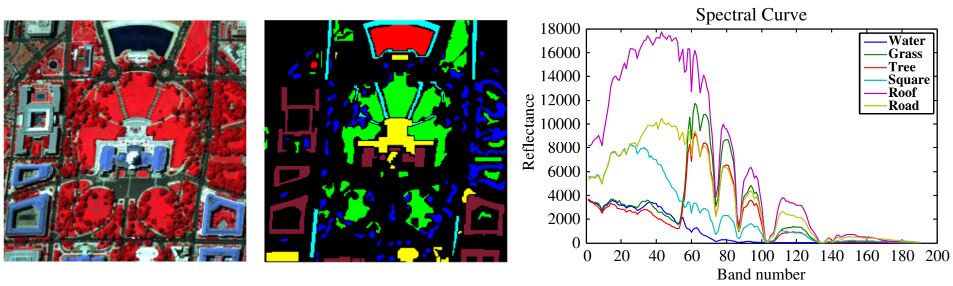

(a) (b) (c)

Fig. 5 HYDICE Washington, DC, Mall image: (a) the false-color image (RGB 63, 52, 36), (b) the ground truth, and (c) the spectral curves of the six land-cover classes.

4.2 *Experimental Settings*

The proposed RMC-OOSSC algorithm was compared with several benchmark clustering methods: k-means,[10] FCM,[11] FCM with spatial information (FCM_S1),[62] the CFSFDP algorithm,[13] the SSC algorithm, and the S^4C algorithm.[22] In addition, a widely used object-oriented method, OOK-means, was also included in the comparison. As the SSC and S^4C algorithms require a lot of memory and have a large computational burden, the experiments were conducted with the help of a computer server. To ensure a fair comparison, all the methods were implemented in MATLAB code under a Linux environment on the server with 32 E5-2630 v3 CPUs at 2.40 GHz and 110 GB of memory, without any parallelization technology. The time unit was seconds.

The original hyperspectral datasets were directly utilized as the input data for all the clustering methods, without any preprocessing. The numbers of clusters for the two experiments were regarded as the prior input parameters, with the other parameters of each clustering method being manually tuned to the optimum, as listed in Table 2. For CFSFDP, the clustering result was obtained through manually selecting the corresponding cluster centers in the decision graph generated by the algorithm. For RMC-OOSSC, in practice, τ was defined as 0.001. To thoroughly evaluate the clustering performance of each method, both the visual clustering result and a quantitative evaluation of the precision [producer's accuracy, user's accuracy, overall accuracy (OA), kappa coefficient, and z-values] are given for each experiment.

4.3 *Experimental Results Obtained with the Reflective Optics System Imaging Spectrometer University of Pavia Dataset*

The clustering maps for the University of Pavia image obtained by k-means, FCM, OOK-means, FCM_S1, CFSFDP, SSC, S^4C, and the proposed RMC-OOSSC algorithm are shown in Fig. 6. The corresponding quantitative evaluation of the clustering precision is provided in Table 3. In the table, the optimal value of each row is shown in bold and the second-best result is in italics.

Through comprehensively analyzing the figure and table, it can be seen that k-means and FCM perform badly in this scene, with significant amounts of misclassifications. For both these methods, the meadows and bitumen classes are not recognized at all. In addition, some of the meadows class is misclassified as bare soil. As a result, k-means and FCM obtain very poor clustering precisions (OA) of 47.99% and 47.54%, respectively. The object-oriented method, OOK-means, effectively improves the clustering performance of k-means. The reason for this is that the object-oriented method can fully exploit the different attributes of the HSI from both the spectral and spatial perspectives, to overcome the defects of the pixel-based methods, such as salt-and-pepper noise. The spatial neighborhood information is also incorporated into the analysis with the help of objects, to utilize the spatial similarity of the spectral signals. For example, the precision of the bitumen class is improved from 58.63% to 59.47%, and the

Table 2 Parameter settings of each method for the two hyperspectral datasets.

Method	University of Pavia	Washington, DC, Mall
K-means	$l = 8$,	$l = 6$,
FCM	$l = 8$, $e = 2$,	$l = 6$, $e = 2$,
FCM_S1	$l = 8$, $e = 2$, $\alpha = 0.2$	$l = 6$, $e = 2$, $\alpha = 0.2$
CFSFDP	—	—
SSC	$l = 8$, $\lambda = 1.3 \times 10^{-5}$	$l = 6$, $\lambda = 5.9 \times 10^{-7}$
S^4C	$l = 8$, $\lambda = 1.3 \times 10^{-5}$, $\alpha = 2.80 \times 10^3$	$l = 6$, $\lambda = 5.9 \times 10^{-7}$, $\alpha = 3.0 \times 10^3$
OOK-means	$l = 8$, $H = 5234$	$l = 6$, $H = 1452$
RMC-OOSSC	$l = 8$, $\lambda = 1.1 \times 10^{-5}$, $H = 5234$	$l = 6$, $\lambda = 4.4 \times 10^{-7}$, $H = 1452$

Note: l, cluster number; e, fuzzy exponential; λ, tradeoff parameter; H, object number; α, tradeoff parameter between the spectral term and spatial term.

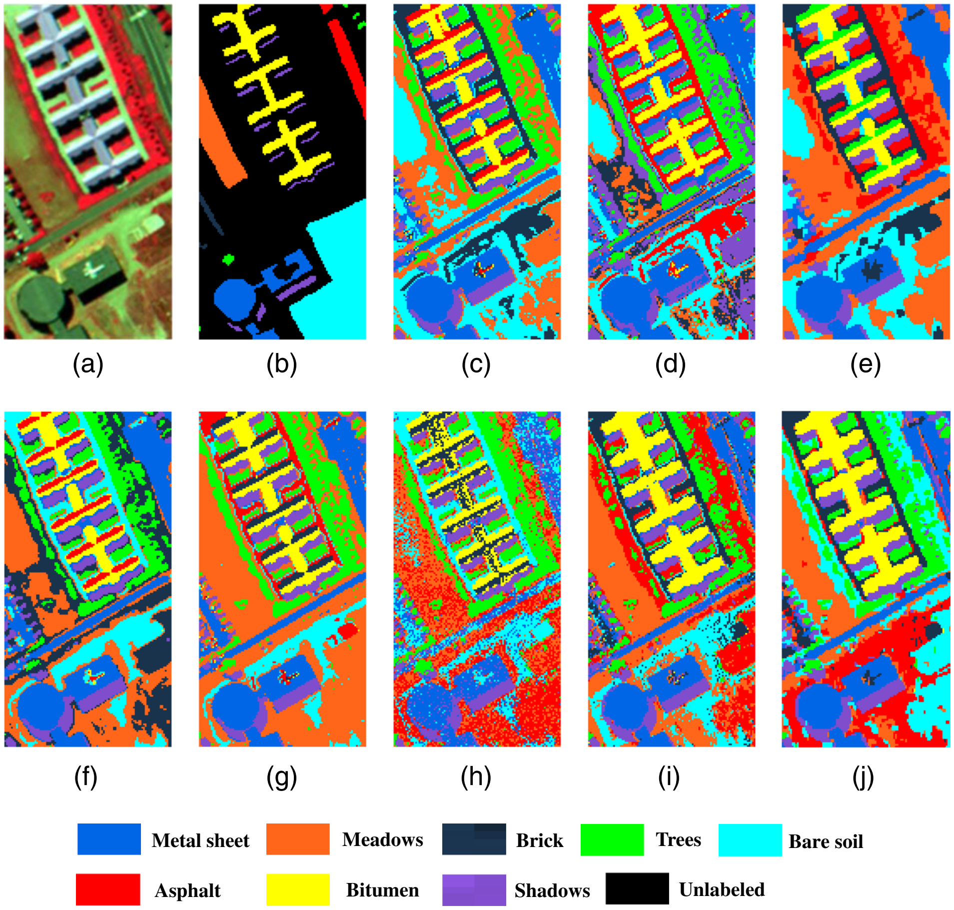

(a) (b) (c) (d) (e)

(f) (g) (h) (i) (j)

Fig. 6 The clustering maps of the different methods for the University of Pavia image: (a) false-color image (RGB 102, 56, 31), (b), ground truth, (c) *k*-means, (d) FCM, (e) OOK-means, (f) FCM_S1, (g) CFSFDP, (h) SSC, (i) S^4C, and (j) RMC-OOSSC.

precision of the meadows class is improved from 21.09% to 40.49%, which illustrates the superiority of the object-oriented method. It can also be seen that FCM_S1 improves the clustering accuracy of FCM to a certain degree because it incorporates the spatial information in the clustering scheme. FCM_S1 can obtain a smoother clustering map than FCM and reduce the misclassification to some degree to achieve a 4.7% increment in OA. CFSFDP can generate a smooth clustering result with a high accuracy, but it still cannot get rid of the defects of the pixel-based methods, with many misclassifications in the clustering map.

We now turn to the three subspace-based methods. SSC obtains a poor performance in this scene. It can be seen that there is much salt-and-pepper noise in the clustering map and a lot of misclassifications, so that the OA is only 43.97%. The bricks, asphalt, and bare soil classes have low precisions at 0%, 0.71%, and 22.04%, respectively. Compared with SSC, S^4C significantly improves the performance to obtain a much better clustering result by simultaneously considering the high correlation among spectra and the spatial neighborhood information.[22] However, the clustering map is not smooth enough, and there is still some salt-and-pepper noise within classes, especially for the bare soil class. This is due to the inevitable defects of the pixel-based methods. Compared with S^4C, the proposed RMC-OOSSC can obtain a smoother clustering result with a higher accuracy. With the help of the object-oriented scheme, the misclassifications can be further decreased and the salt-and-pepper noise problem can be effectively relieved. For example, the precision of the meadows and bare soil classes is improved from 87.30% and 31.93% to 92.06% and 71.28%, respectively. This further proves the superiority of the object-oriented algorithm and the effectiveness of the mass center learning scheme, in which the different neighborhood relationships can be fully utilized to distinguish different land-cover types. As a result, improvements in OA of nearly 28% and 7% are achieved, compared

Table 3 Quantitative evaluations of the different clustering algorithms for the University of Pavia image.

Method	Class	*K*-means	FCM	OOK-means	FCM_S1	CFSFDP	SSC	S^4C	RMC-OOSSC
Producer's accuracy (100%)	Metal sheet	**100**	82.59	97.67	*99.72*	**100**	85.58	99.09	98.95
	Meadows	21.09	25.36	40.49	60.32	74.60	52.60	*87.30*	**92.06**
	Bricks	0	0	3.19	0	0	0	**60.64**	*48.26*
	Trees	66.67	*99.88*	0	87.24	**100**	**100**	98.61	99.72
	Bare soil	*35.05*	27.86	31.14	24.89	20.59	22.04	31.93	**71.28**
	Asphalt	0	0	0	0	0	*0.71*	0	**3.29**
	Bitumen	58.63	76.19	59.47	60.99	60.61	53.84	*98.37*	**99.24**
	Shadows	**100**	57.62	**100**	**100**	*99.87*	98.61	99.09	97.53
User's accuracy (100%)	Metal sheet	65.80	**99.91**	64.47	*98.90*	63.28	48.46	52.41	75.91
	Meadows	12.27	55.95	17.80	**100**	*73.44*	42.84	57.29	73.42
	Bricks	0	0	0.74	0	0	0	*22.44*	**99.20**
	Trees	*91.30*	59.65	0	41.93	**100**	65.13	80.73	75.00
	Bare soil	56.42	39.27	60.75	*96.52*	**99.26**	64.75	96.12	37.22
	Asphalt	0	0	0	0	0	*0.21*	0	**1.28**
	Bitumen	**100**	69.57	**100**	*99.88*	99.62	99.86	71.57	99.69
	Shadows	*97.57*	20.72	99.45	63.00	28.23	58.65	**99.77**	79.85
OA (100%)		47.99	47.54	48.01	52.24	52.12	43.97	*65.09*	**71.98**
Kappa		0.3629	0.3737	0.3736	0.4481	0.4421	0.3495	*0.5852*	**0.6605**
z-value		9.21	7.41	10.81	21.96	20.80	0	*36.60*	**42.37**
Time (s)		*5.1956*	84.4090	**0.2481**	917.4531	280.8706	1.2934E4	7.3983E3	155.4496

with SSC and S^4C, respectively. Another superiority worth mentioning is that the computational time is significantly reduced, from 7.3983×10^3 to 155.4496 s, compared with the S^4C method.

In order to analyze the significant difference between the clustering methods, we took the clustering result of SSC as the baseline and calculated the z-values[63] of the other clustering results. For the widely used 5% level of significance, we consider that there is a significant difference between the two clustering methods if $|z| > 3.84$ holds. From Table 3, it can be clearly observed that the proposed RMC-OOSSC algorithm performs significantly better than the other state-of-the-art methods.

4.4 *Experimental Results obtained with the HYDICE Washington, DC, Mall Dataset*

The clustering maps obtained by each clustering method for the Washington, DC, Mall image are shown in Fig. 7, with the corresponding quantitative evaluation of the clustering precision provided in Table 4. The best result and the second-best result in each row are shown in bold and italics, respectively. From the figure and table, it can be clearly seen that OOK-means effectively improves the performance of k-means by considering the spatial neighborhood information through the object-oriented scheme. FCM_S1 can also obtain a much better clustering result through spatial regularization than FCM. The CFSFDP method generates a smooth clustering

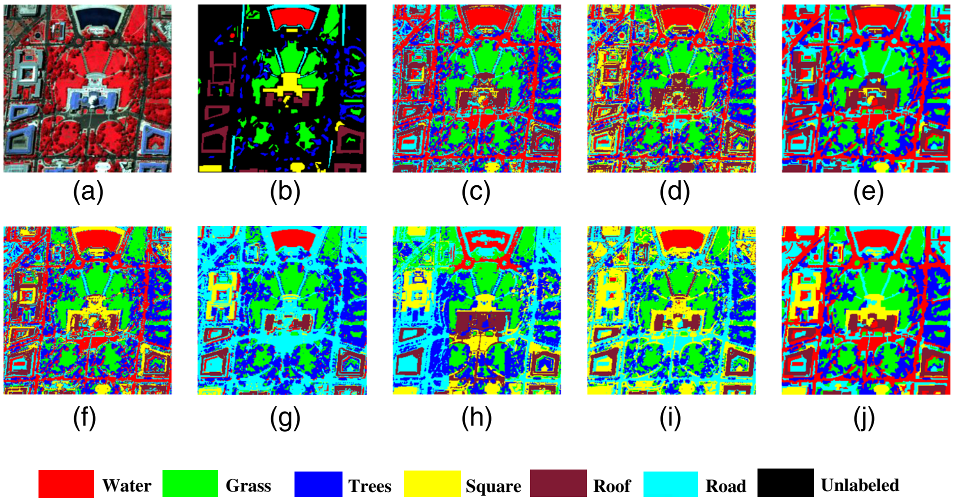
(a) (b) (c) (d) (e)

(f) (g) (h) (i) (j)

Fig. 7 The clustering maps of the different methods for the Washington, DC, Mall image: (a) false-color image (RGB 63, 52, 36), (b), ground truth, (c) *k*-means, (d) FCM, (e) OOK-means, (f) FCM_S1, (g) CFSFDP, (h) SSC, (i) S^{4}C, and (j) RMC-OOSSC.

result, but there are still many misclassifications within each cluster. SSC obtains poor clustering results containing a lot of salt-and-pepper noise and misclassifications in this scene. As a result, the clustering accuracy (OA) is only 81.62%. By simultaneously considering the high correlation among spectra and incorporating the spatial information, S^{4}C effectively improves the performance of SSC to obtain a much smoother clustering map with a higher accuracy. However, there

Table 4 Quantitative evaluations of the different clustering algorithms for the Washington, DC, Mall image.

Method	Class	*K*-means	FCM	OOK-means	FCM_S1	CFSFDP	SSC	S^{4}C	RMC-OOSSC
Producer's accuracy (100%)	Water	**100**	**100**	**100**	**100**	*99.69*	69.29	98.39	**100**
	Grass	98.71	96.91	*98.72*	97.30	95.63	94.95	97.45	**99.70**
	Tree	87.12	88.13	91.53	89.03	**97.05**	88.82	91.85	*93.94*
	Square	26.88	8.38	30.75	80.13	20.49	83.93	**90.73**	*89.90*
	Roof	*87.02*	63.58	**87.91**	79.34	71.61	72.32	76.94	76.56
	Road	36.30	19.09	35.54	20.65	**97.53**	*71.82*	33.33	60.91
User's accuracy (100%)	Water	61.09	65.73	62.18	64.16	*97.22*	86.75	**98.94**	65.14
	Grass	97.13	98.12	*98.72*	98.06	**98.87**	94.18	97.05	98.54
	Tree	65.42	93.14	*96.82*	93.93	91.07	66.59	51.18	**98.98**
	Square	47.26	10.22	53.11	58.85	34.37	77.91	*95.44*	**99.44**
	Roof	*95.05*	50.08	66.28	83.92	**99.89**	56.81	87.30	68.44
	Road	*92.70*	57.54	91.53	58.81	48.04	**99.48**	76.45	84.62
OA (100%)		80.99	72.63	82.54	83.65	83.83	81.62	*85.81*	**89.57**
Kappa		0.7554	0.6485	0.7753	0.7916	0.7953	0.7671	*0.8188*	**0.8673**
z-value		−2.01	−28.02	2.87	7.24	8.66	0	*18.67*	**29.82**
Time (s)		26.6586	361.2703	**0.7603**	2715.1413	8.8179E3	5.8971E4	1.7645E4	*18.8666*

are still some misclassifications and salt-and-pepper noise in the clustering map, especially for the trees, square, and road classes. This is caused by the inherent obstacles faced by the pixel-based clustering methods. Compared with S^4C, the proposed RMC-OOSSC algorithm shows an excellent performance with a higher clustering accuracy. The misclassification and noise are effectively relieved owing to the more powerful discriminative features, i.e., the mass center spectra extracted by the unsupervised learning scheme. For example, the recognition accuracy of road is improved from 33.33% to 60.91% in OA, which further proves the superiority of the object-oriented scheme and the distance reweighted mass center learning scheme. Increments in OA of nearly 8% and 4% are achieved compared with SSC and S^4C, respectively. In addition, it is worth mentioning that the computational time of RMC-OOSSC is significantly reduced from 1.7645×10^4 to 18.8666 s compared with the S^4C method, which is an impressive improvement.

Similarly, we took the clustering result of SSC as the baseline and calculated the z-values of the other clustering results to reflect the significant difference between the clustering methods. From Table 4, it can be clearly observed that the proposed RMC-OOSSC algorithm performs significantly better than the other state-of-the-art methods in this scene.

4.5 *Parameter Analysis*

As the tradeoff between the sparsity of the coefficient and the magnitude of the noise, the regularization parameter λ plays an important role. Therefore, it is necessary to analyze the impacts of different values of λ on the performance of the proposed RMC-OOSSC algorithm. In fact, parameter λ is decided by the following formulation:[21]

$$\lambda = \frac{\beta}{\mu}, \tag{18}$$

$$\mu = \min_{i} \max_{j \neq i} |y_i^T y_j|, \tag{19}$$

where β is the adjustment coefficient and μ is a parameter related to the dataset, which can be explicitly determined.

From Eq. (18), it can be easily concluded that the sensitivity of λ is decided by β in practice, as μ is fixed for a certain dataset. In order to analyze the sensitivity of β, the change trend of the OA of RMC-OOSSC with various values of β for both experimental datasets is shown in Fig. 8. From the figure, generally speaking, it can be easily concluded that the performance of the RMC-OOSSC algorithm is relatively robust with regard to this parameter, and the optimal value always

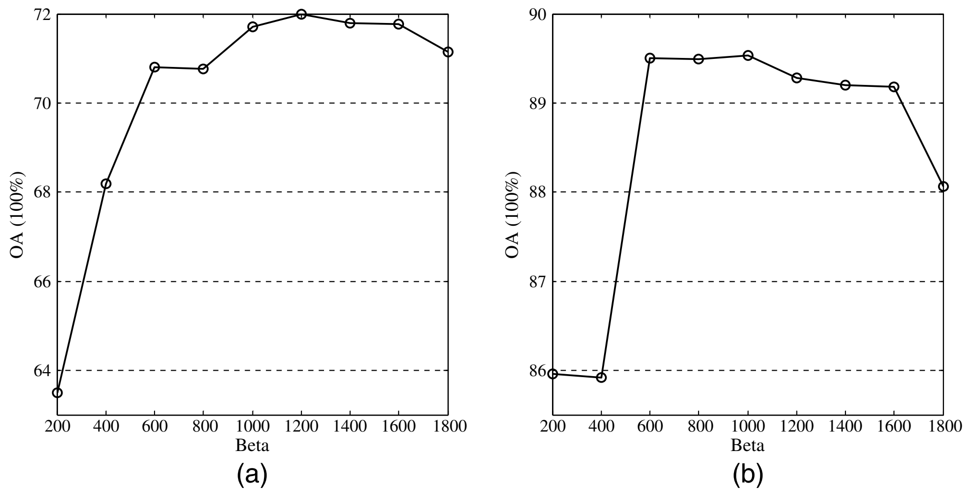

Fig. 8 The analysis of β. The curves show the change trend of the OA of RMC-OOSSC with various values of β for the University of Pavia and Washington, DC, Mall images, respectively. (a) Beta analysis for PaviaU image and (b) beta analysis for DC Mall image.

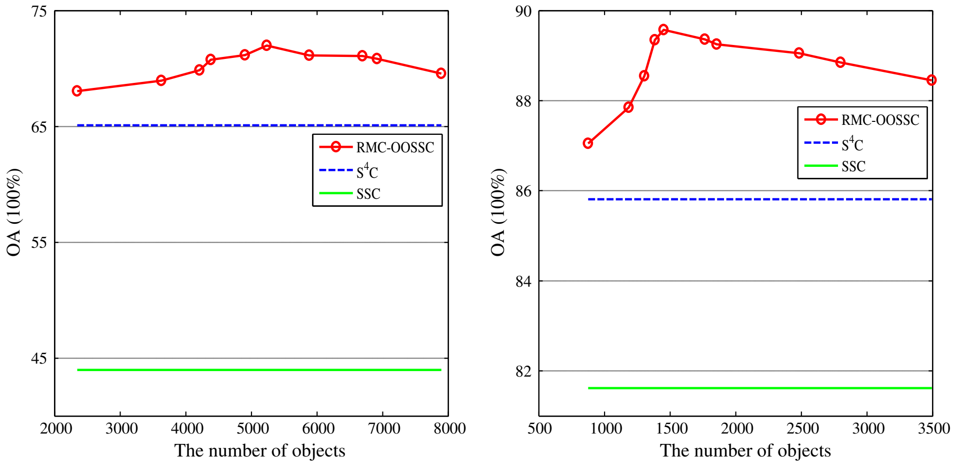

(a) (b)

Fig. 9 Analysis of the number of objects. The curves show the change trend of the OA of RMC-OOSSC with various numbers of objects for the University of Pavia and Washington, DC, Mall images, respectively. (a) Object number analysis for PaviaU image and (b) object number analysis for DC Mall image.

falls in a very narrow range of $[1,2] \times 10^3$. Meanwhile, μ can be explicitly computed with Eq. (19). Therefore, λ is adaptive to the datasets and can be easily fine-tuned.

Compared to the pixel-based algorithms, there is a critical parameter, the number of objects, which controls the clustering accuracy of the proposed RMC-OOSSC algorithm, and its sensitivity should be discussed. As is known to us all, the segmentation degree can have an influence on the final clustering result. Too many objects means redundancy and a high computational burden for a clustering scheme based on sparse representation, while too few objects may cause a challenge for the synergy of the atoms in the sparse representation procedure, which can reduce the clustering accuracy.

As Fig. 9 illustrates, the clustering accuracy of RMC-OOSSC changes with respect to the number of objects over a relatively small range. The accuracy of RMC-OOSSC is always much higher than the pixel-based SSC, and it outperforms the S^4C algorithm for both experimental datasets. For the University of Pavia image, the accuracy of RMC-OOSSC reaches an optimum around 5234 objects. For the Washington, DC, Mall image, the accuracy is the highest around 1452 objects. In general, the performance of the proposed RMC-OOSSC algorithm is relatively robust with respect to the number of objects.

5 Conclusions

In this paper, faced with the problems of the pixel-based clustering methods, we have proposed a distance RMC-OOSSC algorithm for HSIs. By using the mean-shift method to oversegment the HSI, the meaningful objects, which are highly homogeneous, are obtained. An unsupervised distance RMC learning model is then used to extract the representative and discriminative features of the objects and to exploit the spectral–spatial structure of the HSI. Considering the high correlation among the mass center spectra, a weighting scheme is utilized to help the SSC clustering scheme select the corresponding representative atoms to reduce the representation error. The extensive experimental results clearly show that the proposed RMC-OOSSC algorithm obtains a superior clustering performance and significantly reduces the computational time when compared with the pixel-based SSC and S^4C algorithms.

Acknowledgments

This work was supported in part by the National Natural Science Foundation of China under Grants 41571362, 61201342 and 41431175, and by the Fundamental Research Funds for Central

Universities 2015904020202. The authors would like to thank Prof. P. Gamba from the University of Pavia for providing the ROSIS dataset, Prof. D. Landgrebe at Purdue University for providing the free download of the HYDICE image of the Washington, DC, Mall, and Dr. E. Elhamifar and Prof. R. Vidar from Johns Hopkins University for sharing the SSC algorithm code.

References

1. Y. Zhong and L. Zhang, "An adaptive artificial immune network for supervised classification of multi/hyperspectral remote sensing imagery," *IEEE Trans. Geosci. Remote Sens.* **50**(3), 894–909 (2012).
2. S. Chen et al., "Classification of hyperspectral remote sensing imagery by k-nearest-neighborhood simplex based on adaptive C-mutual proportion standard deviation metric," *J. Appl. Remote Sens.* **8**(1), 083578 (2014).
3. R. D. da Silva and H. Pedrini, "Hyperspectral data classification improved by minimum spanning forests," *J. Appl. Remote Sens.* **10**(2), 025007 (2016).
4. H. Huang, "Classification of hyperspectral remote-sensing images based on sparse mainfold learning," *J. Appl. Remote Sens.* **7**(1), 073464 (2013).
5. F. A. Kruse, J. W. Boardman, and J. F. Huntington, "Comparison of EO-1 hyperion and airborne hyperspectral remote sensing data for geologic applications," in *IEEE Aerospace Conf. Proc.*, Vol. **3**, pp. 1501–1513 (2002).
6. J. A. Benediktsson, J. A. Palmason, and J. R. Sveinsson, "Classification of hyperspectral data from urban areas based on extended morphological profiles," *IEEE Trans. Geosci. Remote Sens.* **43**(3), 480–491 (2005).
7. J. A. Palmason et al., "Classification of hyperspectral data from urban areas using morphological preprocessing and independent compont analysis," in *Proc. of IEEE Geoscience and Remote Sensing Symp.*, Vol. **1** (2005).
8. P. K. Goel et al., "Classification of hyperspectral data by decision trees and artificial neural networks to identify weed stress and nitrogen status of corn," *Comput. Electron. Agricul.* **39**(2), 67–93 (2003).
9. A. Plaza et al., "Recent advances in techniques for hyperspectral image processing," *Remote Sens. Environ.* **113**(1), S110–S122 (2009).
10. S. P. Lloyd, "Least squares quantization in PCM," *IEEE Trans. Inf. Theory* **28**(2), 129–137 (1982).
11. J. C. Bezdek, *Pattern Recognition with Fuzzy Objective Function Algorithms*, Springer Science & Business Media, New York city (2013).
12. J. J. Buckley, "Fuzzy hierarchical analysis," *Fuzzy Sets Syst.* **17**(3), 233–247 (1985).
13. A. Rodriguez and A. Laio, "Clustering by fast search-and-find of density peaks," *Science* **344**(6191), 1492–1496 (2014).
14. Y. Zhong, L. Zhang, and W. Gong, "Unsupervised remote sensing image classification using an artificial network," *Int. J. Remote Sens.* **32**(19), 5461–5483 (2011).
15. T. Zhang et al., "Hybird linear modeling via local best-fit flats," *Int. J. Comput. Vision* **100**(3), 217–240 (2012).
16. L. Zelnik-Manor and M. Irani, "Degeneracies, dependencies and their implications in multi-body and multi-sequence factorizations," in *IEEE Conf. on Computer Vision and Pattern Recognition*, p. ll-287 (2003).
17. A. Sarkar, A. Vulimiri, and S. Paul, "Unsupervised and supervised classification of hyperspectral imaging data using projection pursuit and Markov random field segmentation," *Int. J. Remote Sens.* **33**(18), 5799–5818 (2012).
18. E. Elhamifar and R. Vidar, "Sparse subspace clustering: algorithm, theory, and application," *IEEE Trans. Pattern Anal. Mach. Intell.* **35**(11), 2765–2781 (2013).
19. E. Elhamifar and R. Vidar, "Sparse subspace clustering," in *IEEE Conf. on Computer Vision and Pattern Recognition*, pp. 2790–2797 (2009).
20. H. Zhai et al., "Spectral-spatial clustering of hyperspectral remote sensing image with sparse subspace clustering model," in *IEEE GRSS Workshop on Hyperspectral Image and Signal Processing: Evolution in Remote Sensing*, Tokyo, Japan, pp. 2–5 (2015).

21. H. Zhang et al., “Hyperspectral image kernel sparse subspace clustering with spatial max pooling operation,” in *XXIII Congress of the Int. Society For Photogrammetry And Remote Sensing* (2016).
22. H. Zhang et al., “Spectral-spatial sparse subspace clustering algorithm for hyperspectral remote sensing images,” *IEEE Trans. Geosci. Remote Sens.* **54**(6), 3672–3684 (2016).
23. L. Fu, J. Cheng, and Y. Zheng, “Object-oriented classfication of high-resolution remotely sensed imagery,” in *IEEE Conf. on Computer Science & Information Technology*, Vol. **47** (2012).
24. A. F. B. Antunes, C. Lingnau, and J. C. Da Silva, “Object oriented analysis and semantic network for high resolution image classfication,” *Bol. Ciênc. Geodésicas* **9**(2), 233–242 (2003).
25. X. Huang and L. Zhang, “An adaptive mean-shift analysis approach for object extraction and classification from urban hyperspectral images,” *IEEE Trans. Geosci. Remote Sens.* **46**(12), 4173–4185 (2008).
26. G. Das et al., “Rule discovery from time series,” in *Advances in Knowledge Discovery and Data Mining*, pp. 16–22 (1998).
27. B. Hong-Tao et al., “K-means on commodity GPUs with CUDA,” in *WRI World Congress on Computer Science and Information Engineering*, Vol. **3**. pp. 651–655 (2009).
28. K. Navulur, *Multispectral Image Analysis Using the Object-Oriented Paradigm*, CRC press, Florida (2006).
29. A. Struyf, M. Hubert, and P. Rousseeuw, “Clustering in an object-oriented environment,” *J. Stat. Software* **1**(4), 1–30 (1997).
30. U. C. Benz et al., “Multi-resolution, object-oriented fuzzy analysis of remote sensing data for GIS-ready information,” *ISPRS J. Photogramm. Remote Sens.* **58**(3), 239–258 (2004).
31. T. Blaschke et al., “Object-oreinted image processing in an integrated GIS/remote sensing environment and perspectives for environmental applications,” *Environ. Inf. Plann. Polit. Public.* **2**, 555–570 (2000).
32. T. Blaschke, C. Burnett, and A. Pekkarinen, “Image segmentation methods for object-based analysis and classification,” in *Remote Sensing Image Analysis: Including the Spatial Domain*, pp. 211–236, Springer, Netherlands (2004).
33. W. Yi, H. Tang, and Y. Chen, “An object-oriented semantic clustering algorithm for high-resolution remote sensing images using the aspect model,” *IEEE Geosci. Remote Sens. Lett.* **8**(3), 522–526 (2011).
34. L. Wang, W. P. Sousa, and P. Gong, “Integration of object-based and pixel-based classification for mapping mangroves with IKONOS imagery,” *Int. J. Remote Sens.* **25**(24), 5655–5668 (2004).
35. Q. Yu et al., “Object-based detailed vegetation classification with airborne high spatial resolution remote sensing imagery,” *Photogramm. Eng. Remote Sens.* **72**(7), 799–811 (2006).
36. R. L. Kettig and D. A. Landgrebeand, “Classification of multispectral image data by extraction and classification of homogeneous objects,” *IEEE Trans. Geosci. Electron.* **14**(1), 19–26 (1976).
37. D. Comaniciu and P. Meer, “Mean shift: a robust approach toward feature space analysis,” *IEEE Trans. Pattern Anal. Mach. Intell.* **24**(5), 603–619 (2002).
38. E. Elhamifar and R. Vidal, “Clustering disjoint subspaces via sparse representation,” in *IEEE Int. Conf. on Acoustics Speech and Signal Processing*, pp. 1926–1929 (2010).
39. H. Zhai et al., “Squaring weighted low-rank subspace clustering for hyperspectral image band selection,” in *Proc. of IEEE Geoscience and Remote Sensing Symp.*, Beijing (2016).
40. H. Shen and J. Z. Huang, “Sparse principal component analysis via regularized low rank matrix approximation,” *J. Multivar. Anal.* **99**(6), 1015–1034 (2008).
41. Y. X. Wang and H. Xu, “Noisy sparse subspace clustering,” in *Int. Conf. Machine Learning*, No. 1, pp. 89–97 (2013).
42. J. Wright, Y. A. Yang, and A. Ganesh, “Robust face recognition via sparse representation,” *IEEE Trans. Pattern Anal. Mach. Intell.* **31**(2), 210–227 (2009).
43. E. Elhamifar, G. Sapiro, and R. Vidal, “See all by looking at a few: sparse modeling for finding representative objects,” in *IEEE Conf. on Computer Vision and Pattern Recognition*, pp. 1600–1607 (2012).

44. R. Rubinstein, R. Zibulevsky, and M. Elad, “Double sparsity: learning sparse dictionaries for sparse signal approximation,” *IEEE Trans. Signal Process.* **58**(3), 1553–1564 (2010).
45. B. McWilliams and G. Montana, “Subspace clustering of high-dimensional data: a predictive approach,” *Data Min. Knowl. Discovery* **28**(3), 736–772 (2014).
46. S. Zeng et al., “Image segmentation using spectral clustering of Gaussian mixture models,” *Neurocomputing* **144**, 346–356 (2014).
47. U. Von Luxburg, “A tutorial on spectral clustering,” *Stat. Comput.* **17**(4), 395–416 (2007).
48. M. Beauchemin, “A density-based similarity matrix construction for spectral clustering,” *Neurocomputing* **151**, 835–844 (2015).
49. J. Shi and J. Malik, “Normalized cuts and image segmentation,” *IEEE Trans. Pattern Anal. Mach. Intell.* **22**(8), 888–905 (2000).
50. Z. Wu and R. Leahy, “An optimal graph theoretic approach to data clustering: theory and its application to image segmentation,” *IEEE Trans. Pattern Anal. Mach. Intell.* **15**(11), 1101–1113 (1993).
51. G. Zhang, X. Jia, and N. M. Kwok, “Super pixel based remote sensing image classification with histogram descriptors on spectral and spatial data,” in *Proc. of IEEE Geoscience and Remote Sensing Symp.*, pp. 4335–4338 (2012).
52. R. Zabih and V. Kolmogorov, “Spatial coherent clustering using graph cuts,” in *IEEE Conf. on Computer Vision and Pattern Recognition*, Vol. **2**, p. ll-437 (2004).
53. M. Tabbm and N. Ahuja, “Multiscale image segmentation by integrated edge and region detection,” *IEEE Trans. Image Process.* **6**(5), 642–655 (1997).
54. M. Fauvel et al., “Spectral and spatial classification of hyperspectral data using SVMs and morphological profiles,” *IEEE Trans. Geosci. Remote Sens.* **46**(11), 3804–3814 (2008).
55. D. L. Donoho, M. Elad, and V. N. Temlyakov, “Stable recovery of sparse overcomplete representation in the presence of noise,” *IEEE Trans. Inf. Theory* **52**(1), 6–18 (2006).
56. M. Benzi and M. A. Olshanskii, “An augmented Lagrangian-based approach to the Oseen problem,” *SIAM J. Sci. Comput.* **28**(6), 2095–2113 (2006).
57. B. Wahlberg et al., “An ADMM algorithm for a class of total variation regularized estimation problems,” *16th IFAC Symp. System Identification*, Vol. **45**No. 16, pp. 83–88 (2012).
58. C. Chen et al., “The direct extension of ADMM for multi-block convex minimization problems is not necessarily convergent,” *Math. Program.* **155**, 57–79 (2016).
59. J. Eckstein and D. P. Bertsekas, “On the Douglas-Rachford splitting method and the proximal point algorithm for maximal monotone operators,” *Math. Program.* **55**(1-3), 293–318 (1992).
60. D. Gabay and B. Mercier, “A dual algorithm for the solution of nonliear variational problems via finite element approximation,” *Comput. Math. Appl.* **2**(1), 17–40 (1976).
61. J. F. Mota et al., “D-ADMM: a communication-efficient distributed algorithm for separable optimization,” *IEEE Trans. Signal Process.* **61**(10), 2718–2723 (2013).
62. S. Chen and D. Zhang, “Robust image segmentation using FCM with spatial constraints based on new kernel-induced distance measure,” *IEEE Trans. Syst. Man Cybern. B* **34**(4), 1907–1916 (2004).
63. G. M. Foody, “Thematic map comparison: evaluating the statistical significance of differences in classification accuracy,” *Photogramm. Eng. Remote Sens.* **70**(5), 627–633 (2004).

Han Zhai received his BS degree from the School of Surveying and Mapping at Shandong University of Science and Technology, Wuhan, China, in 2014. He is currently pursuing his PhD degree at the State Key Laboratory of Information Engineering in Surveying, Mapping, and Remote Sensing (LIESMARS), Wuhan University, Wuhan, China.

Hongyan Zhang has been an associate professor with the State Key Laboratory of Information Engineering in Surveying, Mapping, and Remote Sensing, Wuhan University, since 2013. He has authored/co-authored more than 50 research papers, with research interests in image reconstruction for quality improvement, hyperspectral image processing, and sparse representation and low rank methods for remote sensing imagery.

Liangpei Zhang is currently the head of the Remote Sensing Division at the State Key Laboratory of Information Engineering in Surveying, Mapping, and Remote Sensing, Wuhan University. He has more than 410 research papers and 15 patents to his name. He won the 2010 Boeing award for best paper and the 2013 ERDAS award for best paper from the American Society of Photogrammetry and Remote Sensing. His research interests include hyperspectral remote sensing, high-resolution remote sensing, image processing, and artificial intelligence.

Pingxiang Li received his BS, MS, and PhD degrees in photogrammetry and remote sensing from Wuhan University, Wuhan, China, in 1986, 1994, and 2003, respectively. Since 2002, he has been a professor with the State Key Laboratory of Information Engineering in Surveying, Mapping, and Remote Sensing (LIESMARS), Wuhan University. His research interests include photogrammetry and SAR image processing.